JOURNAL OF PROPULSION AND POWER
Vol. 16, No. 2, March–April 2000

Two-Dimensional Nonadiabatic Injection into a Supersonic Freestream

Rodney D. W. Bowersox*
University of Alabama, Tuscaloosa, Alabama 35487-0280
and
K. Colin Tucker† and Christopher D. Whitcomb‡
Air Force Institute of Technology, Wright–Patterson Air Force Base, Ohio 45433-7765

Turbulence and mean flow measurements were acquired downstream of a normal, supersonic (Mach 1.6), two-dimensional, slot injection into Mach 2.9 flow ($Re/m = 16 \times 10^6$). An adiabatic ($Tt_i/Tt_\infty = 1.0$) and two nonadiabatic injection cases ($Tt_i/Tt_\infty = 1.11$ and $Tt_i/Tt_\infty = 0.93$) were studied. Multiple-overheat cross-film anemometry and conventional mean flow probes, as well as instantaneous schlieren photography, were utilized to study the turbulent mixing layer. The mean flow data included the pitot, cone-static, and Mach number profiles. The measured turbulence data included Reynolds shear stresses and turbulence intensities (mass flux and total temperature). The flow visualizations highlighted the physical phenomena of the flow as well as the associated turbulent structure that existed in the mixing layer. The injection and wall temperature were found to have a strong influence on the near wall (the bottom-half of the mixing layer relative to the wall) mean and statistical turbulent flow properties.

Nomenclature

a, b	= hot-wire calibration constants
B	= mixing layer width
C_p	= specific heat
h	= enthalpy
M	= Mach number
Nu	= Nusselt number based on hot-film sensor diameter
P	= pressure
Pr	= Prandtl number
q	= heat flux
Re	= Reynolds number
T	= temperature
u, v, w	= velocity components
$\boldsymbol{v}$	= velocity vector
W	= injector throat width
X, Y, Z	= Cartesian coordinates
δ	= boundary-layer height
ρ	= density
τ	= shear stress

Subscripts

i, j	= Cartesian coordinate indices
inj	= injector condition
t	= total condition
wall	= wall condition at X/W equals 72
y	= Y component
1	= local freestream flow condition at X/W equals 72
∞	= wind-tunnel freestream condition

Superscripts

F	= Favre averaged
R	= Reynolds averaged
$\bar{}$	= time-averaged component
$\prime$	= fluctuating component

Introduction

NORMAL injection into a supersonic crossflow is of fundamental and practical interest. This interaction may be identified in several areas including thrust vector control systems inside high-temperature nozzles, boundary-layer and surface cooling of high-temperature flows, and fuel mixing in a supersonic ramjet combustor. Because of the large number of practical applications, two- and three-dimensional jet flows have been the subject of much investigation.[1]

Mixing enhancement in supersonic flow is a key enabling technology in the development of scramjet engines, where the available time to mix the fuel with the incoming air, efficiently combust the mixture, and exit the products will be on the order of milliseconds (Ref. 2). Heiser and Pratt[3] provide empirical mixing efficiencies for three simple mixing schemes with a hydrogen and air mixture, where normal injection was shown to have the potential for relatively high mixing efficiency in the near field.

Computer resources currently limit predictions of complex, high-speed, high Reynolds number, compressible turbulent flows to solutions of an approximate averaged form of the Navier–Stokes equations. Because of the nonlinear nature of the governing equations, this procedure results in additional fluctuation correlation terms, which require modeling. Although not the only limitation, turbulence modeling is currently a controlling factor in the accuracy of all viscous turbulent flowfield solutions.

The development of turbulence models relies heavily on experimental data and physical intuition. A clear lack of quality turbulence data suitable for turbulence model development for high-speed flows has been identified.[4] This sentiment has been echoed for injection-type flows as well.[1] The lack of compressible turbulence data has lead to direct extensions of incompressible models for high-speed flow. Although these models provide reasonably accurate predictions for zero pressure gradient thin-layer-type flows, they have proven unreliable for free mixing layers and shear layers subjected to compression and expansion waves.[5]

Received 26 October 1998; revision received 20 February 1999; accepted for publication 11 March 1999.

*Assistant Professor, Department of Aerospace Engineering and Mechanics. Senior Member AIAA.

†Graduate Research Assistant, Department of Aeronautics and Astronautics; currently Instructor, Department of Aeronautics, U.S. Air Force Academy, Colorado Springs, CO 80840. Member AIAA.

‡Graduate Research Assistant, Department of Aeronautics and Astronautics; currently Aerospace Engineer, U.S. Air Force Research Laboratory PR55.

Motivated by scramjet propulsion, Bowersox and Schetz[6–8] performed experimental studies aimed at providing detailed information concerning the effects of compressibility on the mean and turbulent flow properties of a two-dimensional, high Reynolds number, supersonic tangential mixing layer. Those studies exemplified the importance of compressibility on the mean and turbulent structure of high-speed mixing layer type flow. Reasonably accurate numerical predictions were obtained for this flow using suitable extensions to existing simple algebraic turbulence models.[8]

McCann and Bowersox[9] and Bowersox[10] investigated the mean and turbulent flowfield downstream of low-angled single-port supersonic injection into a supersonic crossflow. Those studies confirmed the strong impact of compressibility; in addition, the numerous secondary vortex flows were also found to significantly alter the turbulent shear stress contours in a nonlinear fashion. An extensive turbulence model evaluation study was performed on this flow using two-equation and Reynolds stress transport models with modern compressibility corrections.[11] In summary, the two-equation model produced shear stress contours that were in poor agreement with the measurements. Neither the contour shape or shear stress magnitudes were accurately simulated. The Reynolds stress transport model produced, at a notable increase in computational cost, a significantly more accurate prediction of the shear stress contour shape and levels. However, significant flowfield differences were present even with this complex level of modeling; for example, the lateral extent of the jet plume was under-predicted by roughly 25%.

The aim of the present study is to provide a characterization of the mean and turbulent flow for a two-dimensional, normal, Mach 1.6 air injection into a Mach 2.9 airstream. In terms of flowfield complexity, this investigation lies between the aforementioned tangential[6–8] and low-angled single-port[9–11] injection studies. In addition to being of practical value, this configuration has many of the flowfield complexities of the three-dimensional study, e.g., compressibility and the shock and expansion interactions. However, the two-dimensional geometry is simple enough to yield this study attractive for turbulence model development efforts. For all cases, air was injected into air. To assess the effects of the injectant temperature on the flow structure, three injection temperatures were tested ($Tt_{inj}/Tt_{\infty} = 0.93$, 1.0, and 1.11). The mean flow profiles ($X/W = 72$) include Mach number, velocity, mass flux, and total temperature. The turbulence profiles include mass flux component turbulence intensities, total-temperature turbulence intensities, turbulent shear stresses, and turbulent heat fluxes. Detailed schlieren flow visualizations were also acquired to provide a clear depiction of the overall flowfield.

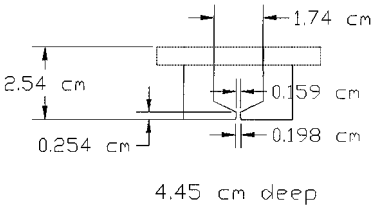

Fig. 1 Scale drawing of the injector model.

Facilities and Instrumentation

Facilities

The experiments were performed in a Mach 2.9 pressure–vacuum wind tunnel located at Wright–Patterson Air Force Base. The freestream Mach number and velocity turbulence intensity were 2.9 ± 0.03 and 0.8%, respectively. The wind-tunnel test section was $6.35 \times 6.35\ \text{cm}^2$. Table 1 summarizes the flow conditions for each of the three experimental configurations. At the injection location, the tunnel ceiling boundary layer, based on pitot pressure data, was approximately 7.0 mm, i.e., $\delta/W = 4.4$. The undisturbed tunnel boundary layers have been shown to be in equilibrium, and detailed mean and turbulence data for the inflow are documented in Ref. 12.

A small two-dimensional converging–diverging nozzle was designed to provide an injector Mach number of 1.6 (based on area ratio). A schematic (drawn to scale) of the injector nozzle is shown in Fig. 1. As indicated, the nozzle throat width W was 1.59 mm. The injector nozzle spanned the center 80% of the tunnel test section, which extended into the boundary layers on each side of the wind tunnel.

A schematic of the experimental setup for the heated-injection case is shown in Fig. 2. As indicated, the injector was located in the tunnel ceiling. The coordinate system was defined such that X was in the freestream flow direction, Y was vertically up (in the laboratory reference frame), and Z completed the right-hand system. The origin was located vertically on the tunnel ceiling, centered axially on the injector exit, and in the spanwise direction, along the tunnel centerline. With this coordinate system, the injectant was directed in the negative Y direction, i.e., down, at the injector exit.

The injectant air was tapped from the tunnel stilling chamber (1.3% of the available air supply). During the present normal operation, the wind tunnel required 67% of the available continuous air supply. Hence, tapping from the tunnel source had minimal affect on the tunnel operation. The heater consisted of 30.5-cm-long Reheat Company, tube-coil-type heater, which produced 329 K continuous airflow. For the cooled-injection case, the heater shown in

Table 1 Wind-tunnel operating conditions

Injection	P_t, kPa	T_t, K	Re/m $\times 10^6$
Adiabatic	204 ± 1.0%	298 ± 0.5%	16 ± 4.0%
Cooled	204 ± 1.0%	295 ± 0.5%	16 ± 4.0%
Heated	202 ± 1.0%	293 ± 0.5%	16 ± 4.0%

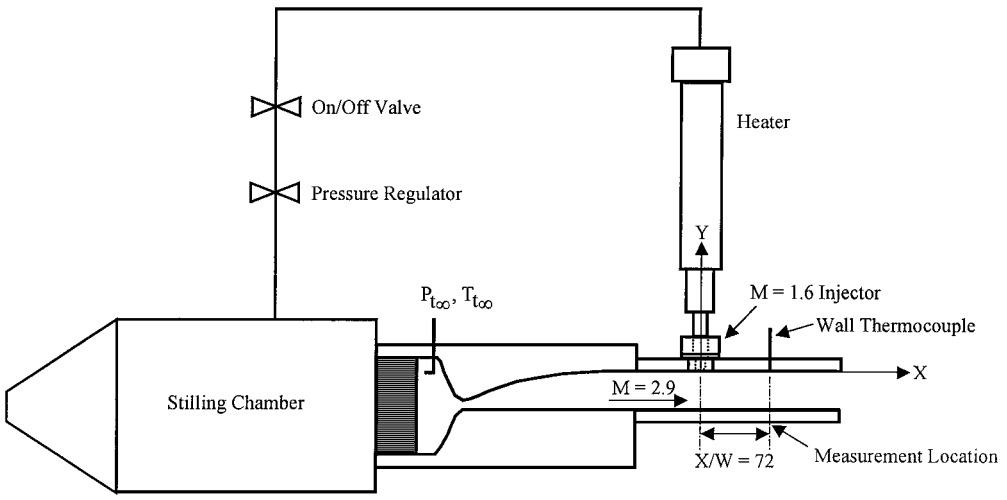

Fig. 2 Schematic of the wind tunnel with the heated injector model.

Table 2 Injector operating conditions

Injection	P_t, kPa	T_t, K	Mass flow, kg/s	u_{inj}/u_∞	ρ_{inj}/ρ_∞	$(\rho u)_{inj}/(\rho u)_\infty$	$(\rho u^2)_{inj}/(\rho u^2)_\infty$
Adiabatic	61.0 ± 1.0%	298 ± 0.5%	0.019 ± 1.0%	0.74	1.25	0.92	0.68
Cooled	61.0 ± 1.0%	273 ± 0.5%	0.018 ± 1.0%	0.71	1.35	0.95	0.67
Heated	65.0 ± 1.0%	329 ± 0.6%	0.018 ± 3.0%	0.78	1.20	0.93	0.73

Fig. 2 was replaced by 15.2-m-long 1.27-cm-diam coiled copper tube that was submerged into a 273 K saline slush. For both the heated and cooled case, the injector and surrounding wall were allowed to achieve and equilibrium temperature before testing began. The wall temperatures were measured during the tunnel operation and were found to remain very close (absolute change of less than 1.5 K) to the equilibrium temperatures. For the adiabatic case, the tapped air went straight into the injector.

The heater power limited the jet mass flow rate. However, it was desired that the conditions also be representative of scramjet fuel injectors.[13] Hence, a compromise between the available total temperature and total pressure resulted in the present test conditions. The injector flow conditions are summarized in Table 2.

Note that the present paper focuses on the influence of injector temperature. However, as indicated in Table 2, the pressure was held nominally constant between the three test cases. Hence, the more conventional correlation variables, namely, the velocity, density, mass flux, and momentum ratios (also listed in Table 2), varied between each flow condition. Although some of the observed phenomena may correlate better with these variables, the jet temperature and heat transfer were the main focus. Also, injecting a dissimilar gas could be used to increase the variation in the more conventional parameters. However, the present hot-film instruments prohibited that option.

Downstream mean flow and turbulence profiles, traversing in the Y direction, were acquired 72 throat widths (114.5-mm) downstream of the injection, i.e., $X/W = 72$, at $Z = 0$. $X/W = 72$ was chosen because the flow angles were small, and thus the measurement uncertainties were minimized. An Y–Z plane Mach number contour was acquired at $X/W = 82$ to document the flowfield two dimensionality.

Instrumentation

The tunnel stagnation conditions were monitored during each run using an Edevco 0.69-MPa pressure transducer and an Omega type-K thermocouple. The conditions were held constant to within the variations shown in Table 1. Similar instruments were used to monitor the injector stagnation conditions. The injector conditions are included in Table 2. The wall temperature at the measurement location was measured with a type-K thermocouple mounted flush with the wall surface. The wall temperatures are summarized in Table 3. Uncertainty analyses, accounting for probe position and transducer calibration uncertainties, were performed for each measurement technique. Table 4 summarizes the uncertainty estimates for the present data.

A conventional single-pass schlieren photography system, with a vertical knife edge, was used. A 10-ns Xenon Corporation light source was used to freeze the flow in the image. Type-57 Polaroid film was used.

Conventional pitot and cone-static pressure profiles were acquired to measure the Mach number. The pitot probe was constructed from a 1.59-mm-outer-diameter stainless steel tube, which was inserted into a 3.18-mm-outer-diameter stainless steel tube. The outer tube was used for reinforcement of the inner tube. Despite this measure, the probes flexed by nominally 0.04 rad during each tunnel run, which was accounted for in the data analysis by assuming that the probe shaft between the support and tip was rigid (~10 cm). With this assumption, the axial and transverse tip displacements were estimated as 0.41 and 0.016 mm, respectively. The vertical probe positions were found to be repeatable to within ±0.1 mm. The opening of the pitot tube was crimped so that the horizontal dimension was approximately twice as large as the vertical dimension. The cone-static probe had a 10 ± 0.03 deg semivertex angle axisymmetric cone machined from stainless steel. The cone tip had four 0.34-mm pressure taps at 90-deg intervals around the circumference and 4.3 mm from the tip of the cone. The pressure taps met in a common chamber, where they were averaged to account for misalignment errors up to ±6.0 deg (Ref. 14). Both the pitot and cone-static pressures were each measured with a 103-kPa Endevco pressure transducer. The combined pitot and cone-static pressure were used to calculate the local Mach number across the mixing layer.[14] The frontal area of each probe was approximately 1.9 mm^2. The measurement uncertainties are listed in Table 4.

Table 3 Local flow conditions, $X/W = 72$

	Adiabatic	Heated	Cooled
Mach[a]	2.8	2.8	2.8
u_1/u_∞ [a]	0.98	0.98	0.99
ρ_1/ρ_∞ [a]	1.04	1.03	1.03
$T_{wall}/T_{t\infty}$	1.02	1.06	0.95

[a] $Y/W = 13$.

Table 4 Uncertainty estimates

Parameter	Uncertainty[a]
δ, B, mm	±0.9
P, $P_{t(\ )}$, % full scale	±0.5
$T_{t(\ )}$, T_{wall}, K	±2.0
Y, mm	±0.1
M	±0.05
u, m/s	±20.0
ρu, kg/m^{2}s	±6.0
$T_t/T_{t\infty}$, %	±2.0
First-order turbulence[b]	±0.007
Second-order turbulence[b]	±0.0006

[a] Representative values at a nominal Mach 2.0.
[b] Normalized by local mean flow.

The probes were traversed at a rate of 0.3 cm/s, and the probe position was monitored with a TransTek, Inc., linear voltage displacement transducer. The data were sampled at a rate 200 Hz with a 12-bit Nicolet data acquisition system. The plotted data points were obtained by averaging blocks of 100 samples.

Turbulence data were acquired using TSI, Inc., 1243-20 platinum cross-film probes. The cross-film probes were instrumented with two 1.0-mm-long, 51-μm-diam wirelike cylindrical hot-film sensors. The cross-film cross-sectional capture area was 0.7 mm^2. The uv probe was aligned to measure flow in the X–Y plane. Limited uw-probe (X–Z plane) data were acquired for the heated injection (model 1243-20AN). Probe attrition prevented additional uw-probe measurements for the adiabatic and cooled-injection configurations.

Multiple-overheat hot-wire anemometry requires at least three overheat ratios to solve for the turbulence intensities and correlations.[15] To obtain accurate turbulence results with multiple-overheat cross-wire anemometry, six overheat ratios, acquired over a series of six tunnel runs (one for each overheat), were used. This is more than the required three and allowed for a least-squares analysis to be applied to the data. The overheat ratios ranged from 1.3 to 1.95. The hot-film probes were traversed at a rate of 0.3 cm/s; data were acquired at a rate of 20 kHz and averaged into blocks of 4096 samples. The anemometer frequency response was optimized to nominally 120 kHz via the square wave technique in the tunnel freestream.

The cross-film data reduction techniques used were developed from the early work of Kovasznay[15] and Spangenberg.[16]

Bowersox[17,18] provides a complete description of the data reduction procedure for multiple-overheat cross-wire anemometry.

In summary, for normal Mach numbers greater that 1.0, experimental cross-wire data have been found to collapse onto the following semi-empirical heat transfer curve:

$$Nu = \left(aRe_e^n + b\right) \tag{1}$$

where Re_e is the effective cooling Reynolds number based on the wire diameter. For the relatively high Reynolds numbers expected in this study ($Re_e > 100$), $n = \frac{1}{2}$ and the cosine law has proven accurate.[18]

Calibration runs were required for each overheat ratio and consisted of placing the probe in the center of the test section with the injector off and then varying the tunnel total pressure from approximately 10–285 kPa. A linear regression was used to obtain the calibration constants a and b in Eq. (1). The minimum linear correlation coefficient was 0.99.

The multiple-overheat cross-wire anemometry data were reduced into scientific form using the generalized least-squares method.[17,18] This method provided the mean mass flux and total temperature, total-temperature and mass flux component turbulence intensities, mass flux component fluctuation cross correlation, and mass flux component total-temperature cross correlations.

The compressible Reynolds shear stress (to second order) given by

$$\tau_{ij}^R = -\overline{\varrho u_i' u_j'} - \bar{u}_i \overline{\varrho' u_j'} - \bar{u}_j \overline{\varrho' u_i'} \tag{2}$$

has been shown to be equivalent (to second order) to the following expression[6,17,18]:

$$\tau_{ij}^R = -\frac{\overline{(\varrho u_i)'(\varrho u_j)'}}{\bar{\varrho}} + \bar{\varrho}\bar{u}_i\bar{u}_j\overline{\left(\frac{\varrho'}{\bar{\varrho}}\right)^2} \tag{3}$$

The first term on the right-hand side of Eq. (3) is directly measured with the cross-wire probe. For thin-layer-type flows, the second term on the right-hand side is usually much smaller than the first. Thus, a direct measurement of the full compressible Reynolds turbulent shear stress, i.e., the summation of the three terms on the right-hand side of Eq. (2), is possible. The relative magnitude of the two terms on the right-hand side of Eq. (3) were compared by applying the uncoupling procedure described in the next paragraph. For all three cases investigated, the second term was only 1–2% of the total; hence, that term was neglected.

Uncoupling the cross-wire results allowed for all of the Reynolds shear stress terms in Eqs. (2) and (3) to be inferred. This procedure involved assuming that the normalized static pressure fluctuations were small compared to those of the density and temperature. Kistler[19] has suggested that the pressure fluctuations were second order and, hence, negligible for wall boundary layers up to Mach 4.7. Furthermore, Bowersox and Schetz[6] demonstrated that the density fluctuation turbulence intensity estimated from cross-wire anemometry, where pressure fluctuations were neglected, were in very good agreement (±5%) with optical measurements. However, the assumption regarding the pressure fluctuations remains controversial. Hence, for the present study, it was only invoked to assess the relative magnitudes of the two terms in Eq. (3) (as discussed in the preceding paragraph).

The transverse component of the turbulent heat flux that results from mass-weighted, i.e., Favre, averaging of the energy equation has been shown[18] to be given by

$$\frac{q_y^F}{\bar{\rho}\bar{u}C_p\tilde{T}_t} = \frac{\overline{(\rho v)' T_t'}}{\overline{\rho u}\tilde{T}_t} \tag{4}$$

The right-hand-side of Eq. (4) is a direct result of multiple-overheat cross-wire anemometry.

Results

Flow Visualization

Shown in Fig. 3 is the schlieren photograph for the heated-injection case. The adiabatic and cooled photographs were virtually identical to that of the heated case; hence, only the heated result is analyzed. Figure 3 provided a highly detailed qualitative view of the salient flow features. First, the injection is visible in the upper left-hand corner of the image, where the injector plume continued to expand as it left the nozzle, and was surrounded by the familiar barrel shock. The jet-induced boundary-layer separation is annotated just upstream of the injection. As indicated, this interaction created a strong jet-induced oblique shock. In addition, a second jet-induced shock formed on the upstream side of the plume, which merged with the main oblique shock. The lighter region below the injection plume is the result of the expansion experienced as the jet flow turned downstream. Through this expansion process, the flow was turned toward the upper surface (or tunnel ceiling). The expanded flow then encountered a recompression shock, which turned the flow parallel to the tunnel ceiling. A second weaker recompression shock was also present and is annotated in Fig. 3. The turbulent mixing layer region defined as the viscous region between the wall and the local freestream and depicted by the large-scale structures that nearly spanned the entire layer is indicated in Fig. 3. The mean flow and turbulence measurements were acquired in this region of the flow.

To clarify for later discussion, the freestream local to the measurement location was defined to be the region between mixing layer and the recompression shock (annotated in Fig. 3). The measured local freestream flow conditions in this region are summarized in Table 3.

Mean Flow Measurements

The mean flow profiles for each injector condition at $X/W = 72.0$ are plotted in Fig. 4. As the mean Mach number (Fig. 4a), velocity (Fig. 4b), and mass flux (Fig. 4c) profiles indicate, the injection produced a thick mixing layer, where the thickness was similar for all three of the injection temperatures ($B/W \cong 9.0$, based on pitot pressure profiles). An interesting feature of the Mach number and velocity data was the smooth profile shape that was similar to a laminar boundary layer. The heated injection (squares on

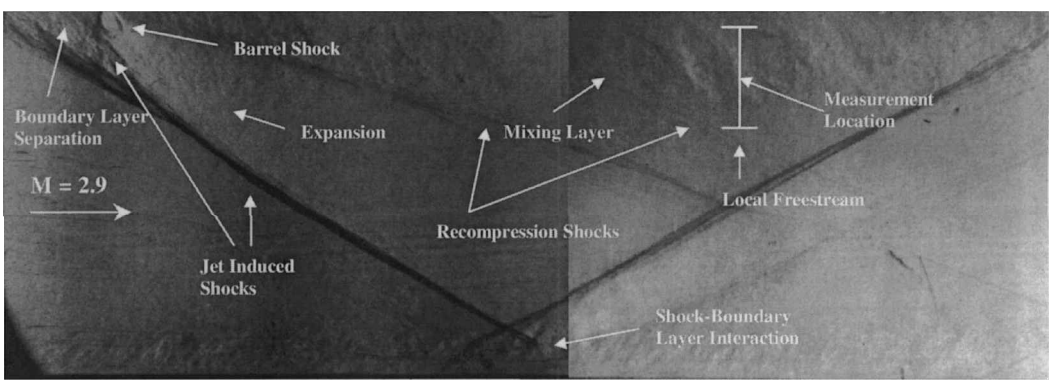

Fig. 3 Vertical knife-edge schlieren photograph of the injector flow (heated injection).

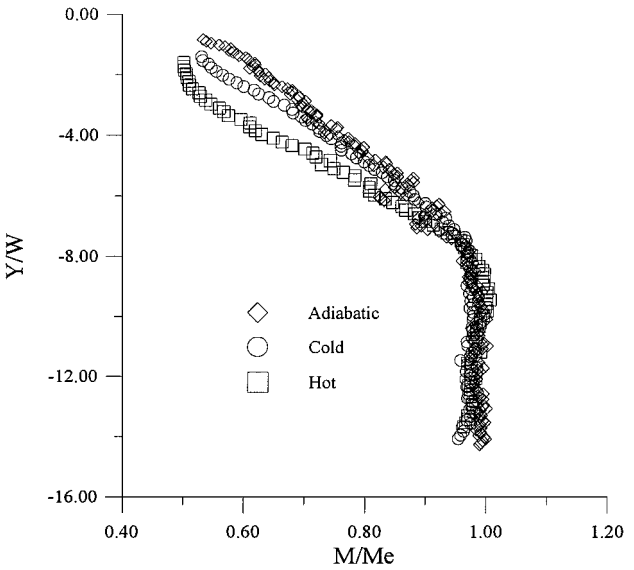

a) Mach number profile, $X/W = 72$

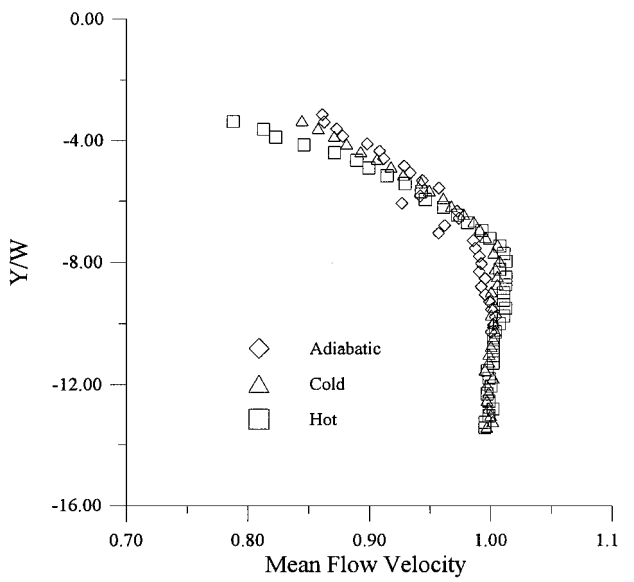

b) Velocity profile, $X/W = 72$

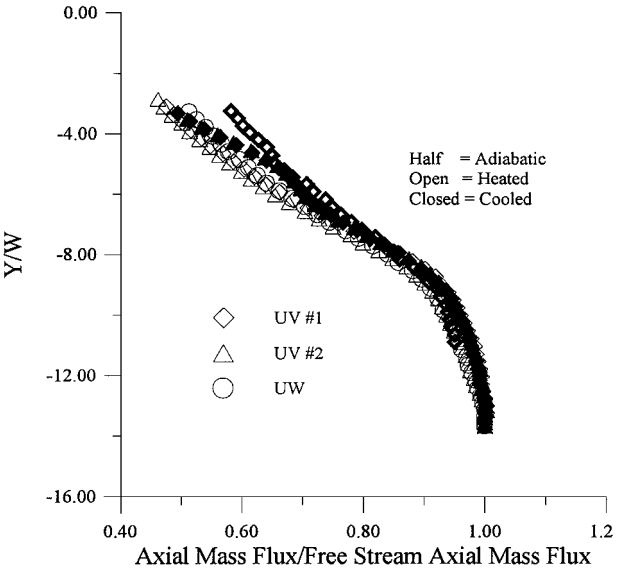

c) Mass flux profile, $X/W = 72$

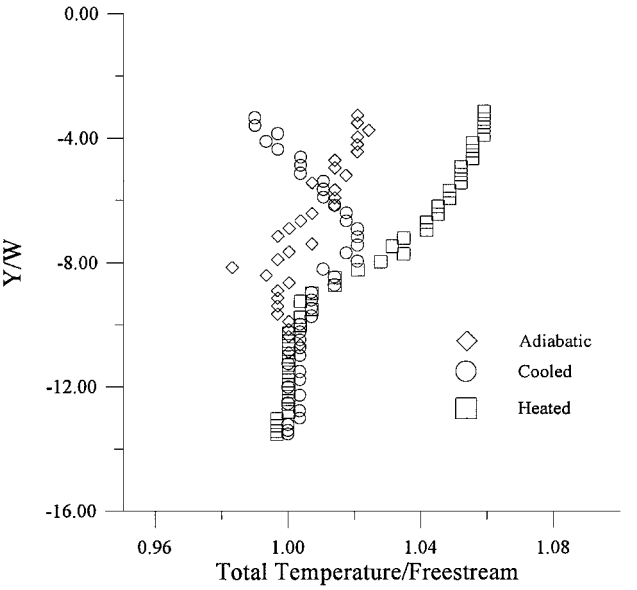

d) Total-temperature profile, $X/W = 72$

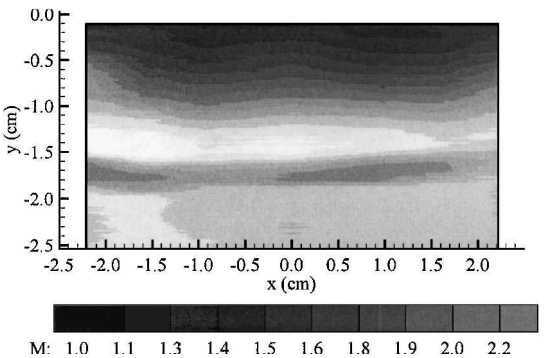

e) Mach contour, $X/W = 82$

Fig. 4 Mean flow data.

Fig. 4a) produced the largest Mach number defect across the entire mixing layer. The cold-injection profile overlapped with the adiabatic case for $Y/W < -3.0$. Closer to the wall, however, the cooled injection produced a larger Mach number defect. The velocity profiles (Fig. 4b), calculated from the Mach number data coupled with the measured total-temperature data (Fig. 4d), show significantly smaller differences between the three cases, which was expected because the momentum ratios were all very similar (last column in Table 2). However, the trend seen in the Mach number plot was conserved. Because both the cooled and heated injection resulted in heat transfer to and from the wall, respectively, the larger velocity defect for each case, i.e., the Reynolds analogy, as compared to the adiabatic injection was expected.

The mean mass flux profiles acquired with the cross-wire probes (Fig. 4c) showed many of the same features measured with the pitot probe. Again, in the outer-half of the mixing layer ($Y/W < -7.0$), the mass flux profiles were independent of injection temperature. However, near the wall significant differences are notable. First, as with the velocity profile, the heated injection (open symbols: triangles, diamonds, and circles) produced the largest defect, and the adiabatic case (half or heavy lined diamonds) produced the smallest defect. Starting from the freestream and moving toward the wall, the cooled-injection profile (solid diamonds and triangles) first followed the adiabatic case, and then at $Y/W \cong -6.0$, the cold-case defect increased to a level that was more consistent with the heated injection. This trend in the mass flux profiles, when taken with the velocity profiles, suggest that the density defect was largest for the cooled-injectioncase. The multiple symbols shown in Fig. 4c for the heated and cooled injection demonstrate that the results were both repeatable and independent of probe type, where the axial mass flux was measured with two uv probes and a uw probe.

The total temperature, for the three injections, varied across the mixing layer as plotted in Fig. 4d. Starting first with the adiabatic case (diamonds), it is apparent that the total temperature increased by 2.0% as the wall was approached. As mentioned earlier, the wall temperatures were measured during each run (summarized in Table 3). The wall temperature, which was equal to the room temperature at the beginning of the run, did not change significantly during the tunnel operation (decreased by nominally 1.5 K). As Table 3 indicates, the wall temperature was 2.0% above the wind-tunnel freestream total temperature. Hence, the increase in the total temperature over the near-wall half of the mixing layer was the result of heat transfer from the wall to the mixing layer.

The total temperature for the heated case (squares in Fig. 4d) also approached the wall temperature (listed in Table 3) in the near-wall half of the mixing layer. Recall the heater and tunnel walls were in a state of thermal equilibrium before the tunnel operation. As with the adiabatic injection case, the wall temperature was nearly constant over the duration of the run (1.5–2.0 K decrease). The cooled-injection (circles in Fig. 4d) total-temperature profile was significantly different than either the heated or adiabatic cases. The total-temperature profile did not level out to the wall value by $Y/W = -3.0$ (as was the case for the heated and adiabatic injections). Instead, the total temperature decreased almost linearly in the mixing layer for $Y/W = -7.0$ to -3.0, and if this trend is linearly extrapolated to the wall, the measured wall temperature (Table 3) is obtained. Hence, $\mathrm{d}(T_t/T_{t\infty})/\mathrm{d}(Y/W)$ was approximately -0.01, which was very small. In addition, the slight increase in the total temperature on the freestream side of the plume (near $Y/W = -8.0$) that resulted from the heat transfer between the cooled-injectionflow and freestream was expected. Hence, the heating on the freestream side of the plume resulted in a mixing layer that was slightly warmer than the wall and, thus, explains the total temperature gradient near the wall.

Shown in Fig. 4e is a contour plot of the Mach number at $X/W = 82$. As the contour indicates, the flowfield was two dimensional over the center 60% of the test section. The variations noticeable in this contour are within the uncertainties listed in Table 4. Thus, the assumption of two dimensionality is reasonable for the present investigation. However, Görtler vortices that frequently result from strong axial pressure gradients could have also contributed to the slight variations noticed in Fig. 4e.

Turbulent Flow Measurements

The mass flux component and total-temperature turbulence intensities for all three injector temperatures are given in Fig. 5a. A probe independenceand flow repeatability study was performed, and as the data in Fig. 5b indicate, the turbulence intensity measurements were repeatable and independent of probe type to within the measurement uncertainties listed in Table 4. Referring back to Fig. 5a, and concentrating first on the axial mass flux turbulence intensities (open symbols), it was noticed that, overall, the turbulence levels for the present study were consistent with the tangential results (peak values of 0.15–0.16) of Bowersox and Schetz[6] and the low-angled injection data (0.10 peak along the centerline) of McCann and Bowersox.[9] However, a systematic influence of the injection temperature on the axial mass flux turbulence levels is discernable in Fig. 5a. First, the heated injection (open squares) produced the highest axial turbulence intensity levels; the peak value was approximately 0.16 at $Y/W = -5.7$. The adiabatic injection (open diamonds) produced the lowest levels, where the peak value at $Y/W = -5.7$ was 0.13. With the exception of the near-wall levels ($Y/W > -7.0$), the profile shapes were very similar for these two cases. The roughly constant axial turbulence intensity difference of 0.04 across the near-wall region corresponds to a 0.04 difference in the total-temperature ratio.

An examination of the energy equation provides a correlation between the turbulence intensity levels and the flow total temperature. Assuming negligible heat transfer, as suggested by the nearly zero total-temperature gradients (Fig. 4d), the energy equation can be written as

$$h_t = h + (\boldsymbol{v} \cdot \boldsymbol{v}/2)$$

Further, assuming a thermally and calorically perfect gas, small static pressure fluctuations, and that $v^2/\bar{u}^2$ and $w^2/\bar{u}^2$ are second order and then performing a binomial expansion for the fluctuating component about the mean and retaining only first-order terms resulted in the following relation between fluctuating components:

$$\frac{T_t'}{\bar{T}_t} = \frac{\bar{T}}{\bar{T}_t}\left(\frac{(\rho u)'}{\overline{\rho u}} - (1 - \bar{M}^2)\frac{\rho'}{\bar{\rho}}\right) \tag{5}$$

Although this equation does not explicitly explain the observed correlation between the axial turbulence intensities and the mean total temperature, it does suggest a relation albeit complicated by the inclusion of two additional flow properties (namely, ρ' and T_t').

The cold injection (open triangles) produced a differently shaped axial mass flux turbulence intensity profile. Near the wall ($y/W > -5.0$), the cold-injectionprofile followed that of the heated case. However, near $Y/W = -5.7$, the cold-injection profile experienced an apparent jump to levels that were closer to the adiabatic case. This trend was also noticed, although not quite as discontinuous, in the mean mass flux profile (Fig. 4c). Referring back to Fig. 4d, the location of this jump also corresponds to the where the adiabatic and cold-flow total-temperature profiles crossed. Because the total temperature fluctuations were nearly the same for all three cases (discussed subsequently), Eq. (5) is applicable to all three cases. Thus, wall heat transfer plays a important role in determining the turbulent flow properties.

Unlike the axial mass flux turbulence data, the transverse mass flux turbulence intensity levels (closed symbols on Fig. 5a) were virtually identical between the three injector configurations across the mixing layer. The thin-layer nature of the present flow explains the observed absence of a correlation between the transverse turbulence intensity levels in Fig. 5a and the total temperature data. Specifically, for thin-layer flows, where $\bar{v}/\bar{u} \ll 1$, the transverse velocity drops out of the fluctuating energy equation [Eq. (5)]. And, for thin-layer flows, the mass flux and transverse velocity fluctuation are related by

$$(\rho v)'/\overline{\rho v} = v'/\bar{v}$$

Thus, the lack of a relation between the total temperature and the transverse mass flux turbulence levels is reasonable.

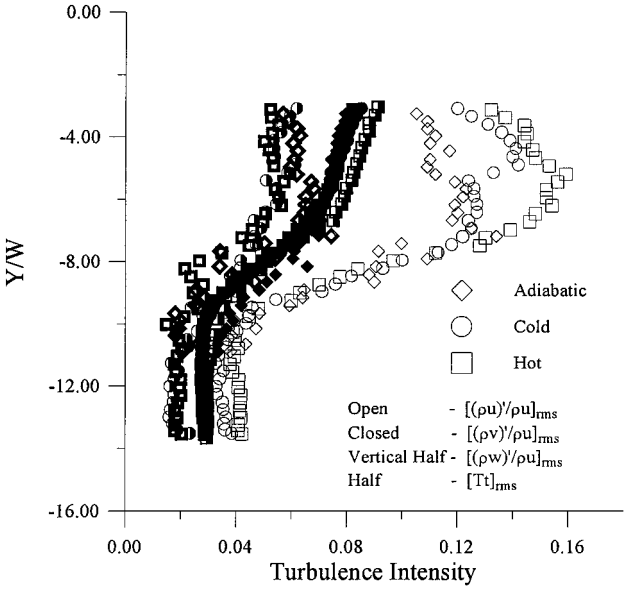

a) Turbulence intensities

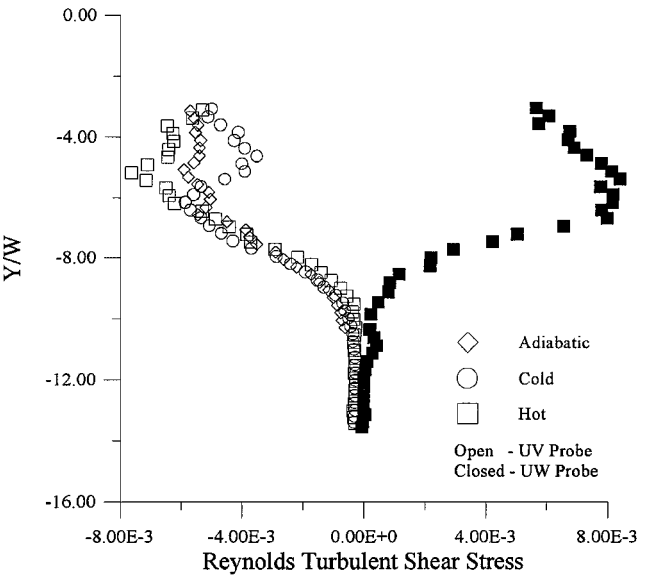

c) Reynolds shear stress

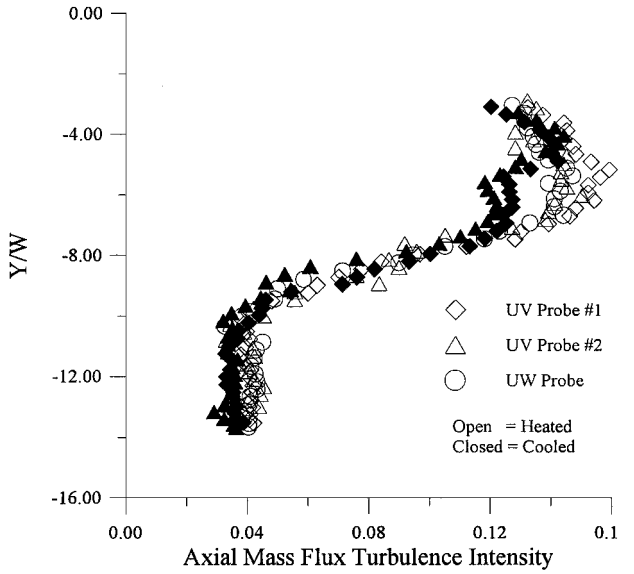

b) Axial mass flux turbulence intensity: repeatability

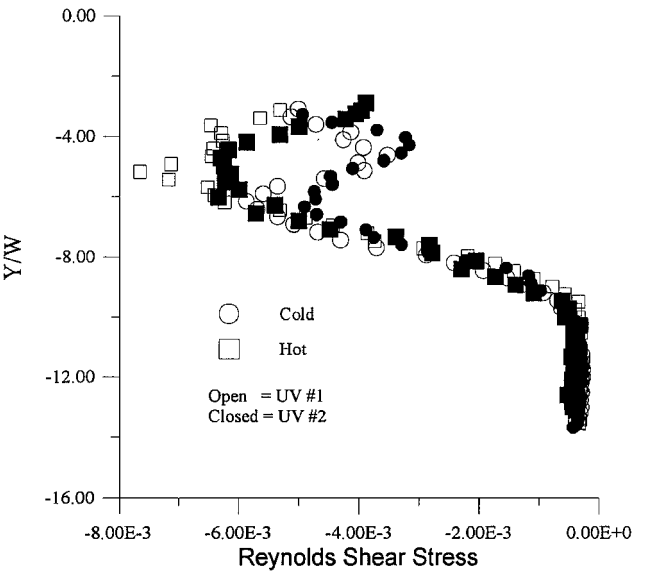

d) Reynolds shear stress: repeatability

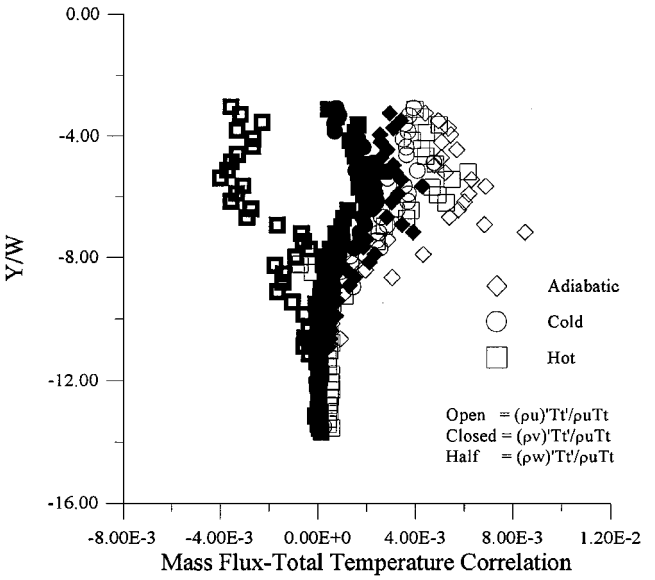

e) Favre heat flux

Fig. 5 Turbulent flow property profiles, $X/W = 72$.

Spanwise mass flux turbulence data were acquired for the heated-injection case only (vertically half-filled squares on Fig. 5a). In the outer mixing layer region, the spanwise and transverse turbulence intensity levels were nearly identical. However, closer to the wall (tunnel ceiling), the spanwise levels were noticeably higher, which indicated that the usual wall damping effects found in boundary layers on the transverse fluctuations were present for the present injection flows.

The total-temperature fluctuation levels are denoted by the heavy-line symbols in Fig. 5a. As the plot indicates, the total-temperature fluctuation levels were nominally 4–5% across the mixing layer and 2% in the freestream for all three injector temperatures. The adiabatic-injection case appeared to have produced slightly higher (~1.0%) total-temperature fluctuation levels; however the differences between the three data sets are within the measurement uncertainty (see Table 4). The present total-temperature fluctuation levels across the mixing layer were nominally 2.0% higher than both the tangential[6] and low-angled single-port injection.[9] This result signifies an increased energy transfer between the jet and freestream for the present normal injection.

The $X-Y$ Reynolds shear stress profiles acquired with the uv probe [Eq. (3)] normalized by the local mean flow properties are presented in Fig. 5c. The chosen coordinate system resulted in the negative Reynolds shear stresses shown. It was also found that the turbulent shear stress measurements, i.e., second-order moments, were repeatable (see Fig. 5d) to within the noted measurement uncertainty (see Table 4). The data in Fig. 5c indicated a strong dependence between the injection temperature and the turbulent shear stress. Multiplying Eq. (5) by $(\rho v)'/\overline{\rho u}$ and averaging results in the following relation:

$$\frac{\overline{(\rho u)'(\rho v)'}}{\overline{\rho u}^2} = \frac{\bar{T}_t}{\bar{T}}\left(\frac{\overline{T_t'(\rho v)'}}{\bar{T}_t\,\overline{\rho u}}\right) - (1-\bar{M}^2)\frac{\overline{\rho'(\rho v)'}}{\bar{\rho}\,\overline{\rho u}} \qquad (6)$$

which demonstrates the dependency of the turbulent shear stresses on the total temperature, i.e., heat transfer, as well as an additional fluctuating correlation. The data in Figs. 5a and 5e (discussed subsequently) indicated that the first term on the right-hand side of Eq. (6) accounted for roughly 40–70% of the total shear stress (left-hand side). Hence, the total-temperature profile, i.e., heat transfer, was an important factor in determining the shear stress distribution.

Concentrating first on the adiabatic turbulent shear stress data (diamonds in Fig. 5c), the magnitude of the turbulent shear stress increased almost monotonically from near zero in the freestream to a nominally constant value of -0.0055 over the bottom 50% of the mixing layer ($Y/W > -5.0$). Referring back to Fig. 4b, note that the velocity profile was nearly linear in this region. Hence, the nearly constant turbulent shear stress measurements are in accordance with the usual mixing length gradient diffusion analogy turbulence models. To qualitatively compare with the present turbulent shear stress data, the mean flow data shown in Fig. 4 were used to estimate the $X-Y$ Reynolds shear stress using the algebraic turbulence model formulation in Ref. 8 at $Y/W = -4.0$. The shear layer width (B/W) was fixed at 9.0. The estimated shear stress with this simple model at this point was within 25% of the present measurement. In addition, the overall levels measured in this study are in good qualitative agreement with those for the tangential[6] and low-angled single-port[9] injections. For those studies, the peak Reynolds shear stress magnitudes were 0.004 and 0.006, respectively. Between $Y/W = -6.9$ and -5.0, the adiabatic turbulent shear stress profile experienced a slight S-shaped variation. Although the magnitude of variation is small and on the order of the measurement accuracy (see Table 4), it is noteworthy because the location corresponds to a similar, more significant, variation in the nonadiabatic-injection shear stress profiles (discussed next).

The heated injection $X-Y$ shear stress profile (squares on Fig. 5c) overlapped with the adiabatic profile for $Y/W < -7.0$. However, moving closer to the wall from that point, significant differences in the shear stress magnitudes are notable. The heated-injection shear stress magnitude peaked near $Y/W = -5.5$ and then decreased in the lower region ($Y/W > -5.0$) to a value of -0.0065 (~ 20% larger than the adiabatic case). The location of the peak corresponded with upper peak in the aforementioned S-shaped variation in the adiabatic-injection profile. The $X-Z$ Reynolds shear stress levels (acquired with the uw probe for the heated case only) were found to be similar in magnitude and opposite in sign to $X-Y$ component. However, the profile shape was slightly different, where the $X-Z$ peak was closer the shear layer freestream interface.

The cold injection produced the most complicated shear stress profile. Like the heated injection, the cold-flow shear stress levels overlapped with the adiabatic data for $Y/W < -5.5$. The maximum cold-injection shear stress was located near the lower peak in the S-shape of the adiabatic-injection profile. Progressing toward the wall, the shear stress magnitudes decreased dramatically with a minimum magnitude value of -0.004 at $Y/W = -4.4$. The shear stress levels then increased to a level consistent with those of adiabatic case at $Y/W = -5.0$.

In summary, the shear stress profiles were found to have strong dependence on the injection temperature as suggested by Eq. (6). The two nonadiabatic-injection shear stress profiles were significantly more complicated than the adiabatic-injection distribution. The complications included local extrema and inflection points. Coupling these complicated shear stress profiles (Fig. 5c) with the monotonic nature of the mean flow profiles (Fig. 4a–4c) indicated that the usual gradient diffusion models would not be adequate for the nonadiabatic injections.

The mass flux total-temperature fluctuation correlation [Eq. (4)] data are plotted in Fig. 5e. A systematic dependence on the injection temperature was unattainable from these data. This lack of dependence is reasonable considering that the turbulent heat fluxes are often modeled as being proportional to total-temperature gradient,[8] which were very small for all three of the injection temperatures. On the other hand, the relative magnitudes of the three components are readily discernable. As indicated in Fig. 5e, the axial (open symbols) and transverse (closed symbols) correlation components were positive across the mixing layer. The axial component values were nominally twice the transverse correlation data. The spanwise component data (heavy open squares) were negative across the layer, which agreed with Ref. 7, and the magnitudes were similar to those of the axial component.

Conclusions

An experimental investigation of the effects of mild injection temperature variations on the mean and turbulent flowfield properties in the far field ($X/W = 72$) of two-dimensional supersonic ($M = 1.6$) air injection into a high Reynolds number supersonic ($M = 2.0$, $Re/\mathrm{m} = 16 \times 10^6$) crossflow was performed at three temperature ratios ($Tt_{\mathrm{inj}}/Tt_{\infty} = 0.93$, 1.0, and 1.11). In general, the results describe in detail the influence of injection temperature on the mean and turbulent statistical flow properties of a highly compressible turbulent mixing layer, which are of both practical and theoretical interests. In summary, the results demonstrated that the heat transfer across the flow significantly influenced the mean and turbulent flow profiles.

In particular, the following observations concerning the influence of the injection temperature on the mean and turbulent flow properties for the present study were drawn. First, the flow property profiles were found to be independent of the injection temperature in the outer- (freestream side) half of the mixing layer. However, in the lower-half (nearer to the wall) significant differences were noted. Specifically, the heated case produced the large defect in Mach number, velocity, and mean mass flux, where the adiabatic injection produced the smallest. Second, the total-temperature profiles demonstrated a strong and complicated dependency on injection temperature, which was found to correlate with the observed trends in the turbulence data. Third, heating the injectant increased the axial mass flux turbulence intensity levels across the lower-half of the mixing layer by 30%. Cooling the injectant produced a complicated axial turbulence intensity profile, where a nearly discontinuous jump in the turbulence levels was observed. Fourth, the transverse mass flux intensity levels were, as expected, unaffected by the injection temperature. Fifth, limited spanwise data confirmed the wall

damping effect on the transverse data. Sixth, heating and cooling the injectant produced complicated Reynolds shear stress profiles, as compared to the adiabatic injection. It is expected that current gradient-diffusion turbulence models are not suited to model these flows. Finally, the turbulent heat flux was found to be independent of the injection temperature, which, because of the small observed total-temperature gradients, was the expected result.

Acknowledgments

The authors thank A. Nejad of the U.S. Air Force Wright Laboratory and T. Chen of Taitech, Inc., for sponsoring this work.

References

[1]Margason, R., "Fifty Years of Jets into a Crossflow Research," 72nd AGARD Fluid Dynamics Panel Meeting, Special Course on Missile Aerodynamics, AGARD-CP-534, Nov. 1993, pp 1.1–1.41.

[2]Fuller, E., Mays, R., Thomas, R., and Schetz, J., "Mixing Studies of Helium in Air at High Supersonic Speeds," *AIAA Journal*, Vol. 30, No. 9, 1992, pp. 2234–2243.

[3]Heiser, W. H., Pratt, D. T., *Hypersonic Airbreathing Propulsion*, AIAA, Washington, DC, 1994, pp. 280–313.

[4]Settles, G. S., and Dobson, L. J., "Supersonic and Hypersonic Shock/Boundary-Layer Interaction Database," *AIAA Journal*, Vol. 32, No. 7, 1994, pp. 1377–1383.

[5]Liou, W., and Shih, T., "On the Basic Equations for the Second Order Modeling of Compressible Turbulence," NASA TM 105277, Oct. 1991.

[6]Bowersox, R., and Schetz, A., "Compressible Turbulence Measurements in a High-Speed High-Reynolds Number Mixing Layer," *AIAA Journal*, Vol. 32, No. 4, 1994, pp. 758–764.

[7]Bowersox, R., and Schetz, A., "Measurements of Compressible Turbulent Flow Structure in a Supersonic Mixing Layer," *AIAA Journal*, Vol. 33, No. 11, 1995, pp. 2101–2106.

[8]Bowersox, R., and Schetz, A., "A Model for Compressible Turbulence in Hypersonic Wall Boundary and High-Speed Mixing Layers," *AIAA Journal*, Vol. 32, No. 7, 1994, pp. 1531–1533.

[9]McCann, G., and Bowersox, R., "Experimental Investigation of Supersonic Gaseous Injection into a Supersonic Freestream," *AIAA Journal*, Vol. 34, No. 2, 1996, pp. 317–323.

[10]Bowersox, R., "Turbulent Flow Structure Characterization of Angled Injection into a Supersonic Crossflow," *Journal of Spacecraft and Rockets*, Vol. 34, No. 2, 1997, pp. 205–213.

[11]Chenault, C., Beran, P., and Bowersox, R., "Second-Order Reynolds Stress Turbulence Modeling of Three-Dimensional Oblique Supersonic Injection," AIAA Paper 98-3425, July 1998.

[12]Bowersox, R., and Buter, T., "Mass-Weighted Turbulence Measurements in a Mach 2.9 Boundary Layer with Mild Adverse and Favorable Pressure Gradient," *AIAA Journal*, Vol. 34, No. 12, 1996, pp. 2470–2483.

[13]Drummond, J., and Weidner, E., "Numerical Study of Scramjet Engine Flowfield," *AIAA Journal*, Vol. 20, No. 9, pp. 1182–1187.

[14]Volluz, R., *Handbook of Supersonic Aerodynamics*, Sec. 20, Wind Tunnel Instrumentation and Operation, NAVORD Rept. 1488, Vol. 6., Ordnance Aerophysics Lab., Daingerfield, TX, 1961.

[15]Kovasznay, L., "The Hot-Wire Anemometer in Supersonic Flow," *Journal of the Aeronautical Sciences*, Vol. 17, Sept. 1950, pp. 565–584.

[16]Spangenburg, W., "Heat-Loss Characteristics of Hot-Wire Anemometers at Various Densities in Transonic and Supersonic Flow," NACA TN 3381, May 1955.

[17]Bowersox, R., "Thermal Anemometry," *Handbook of Fluid Mechanics and Fluid Machinery*, Wiley, Sec. 15.4.2, Dec. 1995, pp. 15.29–15.40.

[18]Bowersox, R., "Combined Laser Doppler Velocimetry and Cross-Wire Anemometry Analysis for Supersonic Turbulent Flow," *AIAA Journal*, Vol. 34, No. 11, 1996, pp. 2269–2275.

[19]Kistler, A., "Fluctuation Measurements in a Supersonic Turbulent Boundary Layer," *Physics of Fluids*, Vol. 2, No. 3, 1959, pp. 290–296.